



Article

Reducing Oxidation during Direct Metal Deposition Process: Effects on Ti6Al4V Microstructure and Mechanical Properties

Dominik Keller * and Konrad Wegener

Institute for Machine Tools and Manufacturing, ETH Zurich, Leonhardstrasse 21, 8092 Zurich, Switzerland

* Correspondence: keller@iwf.mavt.ethz.ch

Abstract: The production of materials with a high affinity for oxidation using the direct metal deposition (DMD) process requires an extended process examination that goes beyond the usual, purely energetic consideration, with the aim of providing sufficient energy to melt the substrate and the powder material supplied. This is because the DMD process does not allow any conclusions to be drawn as to whether it and its respective selected parameters result in an oxidation critical process. To assess this, a superposition of the temperature field with the existing spatial oxygen concentration is required. This work uses this approach to develop an oxidation model that reduces oxidation during the DMD process. In addition to the numerical model, an analytical model is derived, with which the temperature of a material element can be calculated analytically and the resulting boundary oxygen concentration calculated using Fick's 2nd law. The model also takes into account two-stage oxidation kinetics for Ti alloys. The effect of too high a travel speed (with the same specific energy of the other experiments) is shown visually in the numerical calculation of the temperature field. However, if the process model is taken into account, the components do fulfil the specified requirements. Finally, the effect of oxidation on the microstructure, microhardness, ultimate strength, yield strength and elongation at failure of Ti6Al4V structures produced using DMD is also investigated, and further supports our conclusions regarding the effectiveness of the proposed model.

Keywords: oxidation; direct metal deposition (DMD); modelling; titanium; oxygen uptake; temperature field; simulation



Citation: Keller, D.; Wegener, K. Reducing Oxidation during Direct Metal Deposition Process: Effects on Ti6Al4V Microstructure and Mechanical Properties. *J. Manuf. Mater. Process.* **2024**, *8*, 89. <https://doi.org/10.3390/jmmp8030089>

Academic Editor: Andrea Ghiotti

Received: 17 March 2024

Revised: 23 April 2024

Accepted: 23 April 2024

Published: 28 April 2024



Copyright: © 2024 by the authors. Licensee MDPI, Basel, Switzerland. This article is an open access article distributed under the terms and conditions of the Creative Commons Attribution (CC BY) license (<https://creativecommons.org/licenses/by/4.0/>).

1. Introduction

Additive manufacturing (AM) represents a pioneering field in manufacturing, distinct from traditional processes, offering novel research avenues and industrial potentials. The advantages of additive manufacturing processes lie in the areas of customisability, quantity, flexibility and geometric design freedom [1,2]—the latter also known as “complexity for free”, as geometrically complex components can be realised without additional process time, costs and assembly, compared to conventional manufacturing processes (e.g., milling, turning, drilling, casting, etc.). Additive manufacturing processes can be differentiated on the basis of the feedstock and the energy source that is available as a heat source for processing. An overview of the categorisation of the individual manufacturing processes can be found in the work of Dass and Moridi [3].

This paper deals with the direct metal deposition (DMD) process, in which a melt pool is created on a substrate using a laser, and the material to be deposited, which is in powder form, is fed in using a powder nozzle. The focus of research has been on finding process windows and specifying the microstructure and mechanical properties for Fe- and Ni-based alloys [4–7], but not in creating a nearly oxidation-free process. This is important, however, as Ti alloys and, surprisingly, steels such as the martensitic steel 1.4313 exhibit strong oxidation under uncontrolled conditions [8]. A process window can be found by

varying the primary process parameters of laser power, travel speed, mass flow rate and laser spot diameter. The introduction of the line energy E_l is as follows:

$$E_l = \frac{P}{v} \quad (1)$$

where P is the laser power and v is the travel speed. The quotient of the line energy can be extended by the laser spot diameter s , so that the specific energy E_s (the energy input per area with the unit J/mm^2) can be calculated as follows:

$$E_s = \frac{P}{s \cdot v} \quad (2)$$

A sufficiently high specific energy is necessary to avoid the lack of fusion between the substrate and the additive structure and reduce the porosity of the additive structure [9]. For oxidation-critical materials (e.g., Ti and its alloys, Al and its alloys, and some steels, e.g., soft martensitic stainless steels (1.4313)), finding a process window from an energetic perspective alone is insufficient, as oxidation worsens the mechanical properties of these materials (e.g., the embrittlement of titanium [10]). Titanium, in particular, has a high affinity for oxygen; therefore, the oxidation behaviour of this material and its alloys must be investigated in more detail.

Due to the high reactivity of titanium with oxygen, a well-adhering oxide layer (OL), a few nanometres thick, forms on the surface, even at room temperature [11]. This leads to good chemical resistance in corrosive media and makes titanium, with its biocompatible properties, suitable for medical technology [12]. The surface oxide usually has the composition TiO_2 [13–16]. Gurappa's work shows that a hard, brittle oxygen diffusion zone (ODZ) forms under the oxide layer, which leads to low fatigue resistance and the reduced tensile strength of the titanium deposit [17]. The oxidation kinetics that result from parabolic oxidation can be described with an oxide–metal diffusion model, according to Wallwork [18]. The oxide formed during oxidation has the thickness d , which is proportional to the square root of the time t and the diffusion coefficient D_{Ox} of oxygen within the surface oxide layer formed. This means that the thickness of the oxide layer can be mathematically described by the following equation:

$$d = 2 \cdot \sqrt{D_{Ox} \cdot t} \quad (3)$$

An oxygen gradient is present in the oxide layer, which decreases from c_{Ox0} to c_{Ox1} . The interstitial concentration of oxygen dissolved in the titanium structure can be described by the error function, whereby the maximum oxygen concentration at the oxide–metal interface corresponds to the maximum solubility of oxygen in the metal c_{M1} . The mathematical representation of the spatial and temporal evolution of the dissolved oxygen in the titanium structure follows the below equation:

$$c(x, t) = c_{M1} + b \left(1 - \operatorname{erf} \frac{x}{2 \cdot \sqrt{D_M \cdot t}} \right) \quad (4)$$

where b is a constant, x is the distance to the metal–oxide interface and D_M is the diffusion coefficient for oxygen within the metal. It should be noted that these formulae only apply to oxidation after the formation of an oxide layer. Guleryuz and Cimenoglu have investigated the oxidation kinetics of Ti6Al4V for temperatures in the range of 600–800 °C and oxidation times in the range of 0.5–72 h [19]. The oxidation kinetics can be described by the following equation:

$$\frac{\Delta W}{A} = K \cdot t^{\frac{1}{n}} \quad (5)$$

where $\frac{\Delta W}{A}$ is the normalised weight gain with regard to the oxidation surface, K is a rate constant, t is the oxidation time and n is the reaction index. For temperatures below 700 °C, a parabolic oxidation (n equals 2) is observed, and, for temperatures above 700 °C, a linear oxidation kinetic (n equals 1) is observed. The results of this study are supported by various

studies. Yu et al. observed an increased, linear oxidation rate at 700 °C after 20 h due to the failure of the oxide layer [20]. Coddet et al. [21] also showed that the adhesion strength of the oxide layer is nearly zero for temperatures higher than 700 °C, leading to increased oxidation rates.

The above-mentioned results of the oxidation kinetics of titanium show only limited suitability for the DMD process. This can be explained by the following typical DMD process characteristics:

- High-temperature oxidation in the range of the melting point of Ti, i.e., at 1670 °C and higher, can only be determined for oxidation times of several minutes or hours for isothermal oxidation. However, the DMD process does not exhibit isothermal temperature fields, but transient temperature fields with high cooling rates.
- The temperature fields are influenced by various process characteristics (e.g., laser power, travel speed, mass flow, etc.) and material parameters such as the thermal conductivity of the material. The temperature field of the DMD process is characterised by the fact that a material element is exposed to rapidly and strongly changing temperatures, which also results in a change in the local diffusion coefficient.

The aim of this work is to model the oxidation of the DMD process at typical DMD temperature fields. These must be superpositioned with local spatial oxygen concentration distributions. For this purpose, temperature fields are calculated numerically, with which an oxidation model can be created with the help of the oxygen concentration simulation and oxygen measurement, according to [22], and the resulting oxygen uptake, which is described in the work of Keller et al. [23]. Furthermore, the effect of oxidation on the microstructure, microhardness and mechanical properties is analysed.

2. Materials and Methods

The experiments were carried out with a Ytterbium-YAG laser (TruDisk 3001). This has a wavelength of 1030 nm with a maximum output power of 3 kW. The specification of the wavelength is important for the numerical simulation in the next Section, as the absorption of a material depends on the wavelength. The absorption coefficient is one of the input parameters for the numerical simulation. Ti6Al4V substrates are used, onto which Ti6Al4V powder is fed into the process using a ring slit nozzle (ILT (Institute for Laser technology) Coax 40 S). Ti6Al4V belongs to the class of titanium alloys known as alpha–beta alloys. These alloys contain of a mixture of both alpha (α) and beta (β) phases at room temperature. The addition of aluminium and vanadium promotes the formation of both phases, contributing to the alloy’s desirable combination of mechanical properties. The chemical composition of the powder, which was produced by Oerlikon Metco, is shown in Table 1.

Table 1. Chemical composition of the substrate and powder material in weight percentage.

	Ti	Fe	C	H	O	N	Al	V
Substrate	Bal.	0.17	0.013	0.002	0.115	0.0045	6.25	4.09
Powder	Bal.	0.24	0.002	0.002	0.05	0.004	6.34	4.25

The powder was transported to the powder nozzle by means of a powder feeder via antistatic hoses using a carrier gas flow. The stand-off between the powder nozzle and the substrate was 7 mm. The powder was produced using a gas atomisation process and its particles were mostly spherical, as shown in Figure 1.

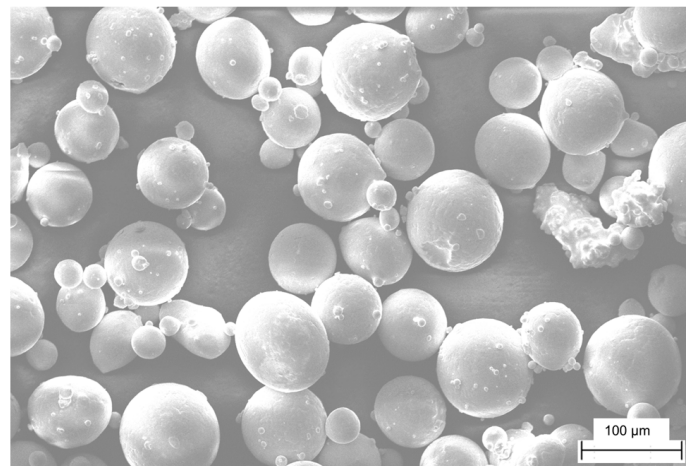


Figure 1. Scanning electron microscope (SEM) image (image taken at 400× magnification) of the used Ti6Al4V powder for the DMD experiments [23].

Argon was used as a carrier gas and shielded gas species. The impurities of the argon gas consisted of H₂O (5 bar) < 3 ppm, O₂ < 2 ppm, N₂ < 10 ppm, CH₄ < 1 ppm and CO₂ < 1 ppm. The measurement of the particle size distribution was conducted through laser diffractometry using the Bettersizer S2 instrument. The results of the measurements are shown in Figure 2.

D03 = 45.14 (μm)	D06 = 50.45 (μm)	D10 = 54.69 (μm)	D16 = 59.58 (μm)	D25 = 65.69 (μm)
D75 = 96.59 (μm)	D50 = 80.01 (μm)	D84 = 106.2 (μm)	D90 = 115.1 (μm)	D97 = 135.5 (μm)

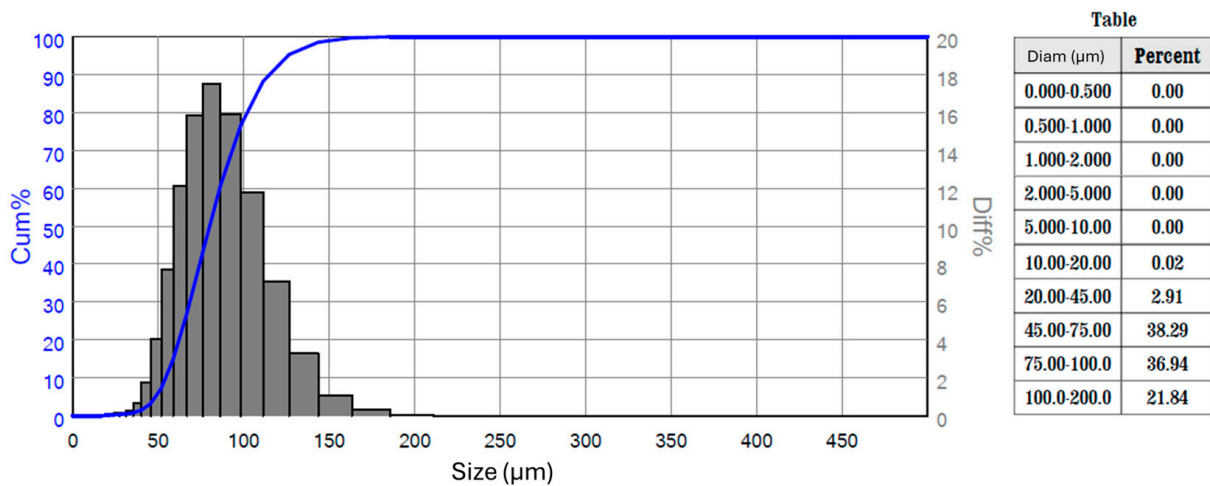


Figure 2. Particle size distribution of the powder used for the experiments. Cumulative percentage (Cum%) refers to the proportion of particles smaller than a particular micron size. On the other hand, the term “differential percentage” (Diff%) denotes the proportion of particles that have exactly that micron size.

The methodology follows a similar approach to the experiments conducted by Keller et al. [23]. However, only those experiments performed using a ring slit nozzle were selected. The process parameters of the respective experiments are presented in Table 2.

Table 2. Experimental plan for investigating the effects of gas flow settings, shield gas chamber utilisation, travel speed and a heat sink (as shown in Figure 3) on oxidation during the DMD process.

Laser Power [W]	Travel Speed [mm/min]	Powder Mass Flow [g/min]	Laser Spot Diameter [mm]	Carrier Gas Flow [L/min]	Shield Gas Flow [L/min]	Shield Gas Chamber	Heat Sink
1100	720	4	3	4	15	no	no
1100	720	4	3	4	30	no	no
1100	720	4	3	8	15	no	no
1100	720	4	3	8	30	no	no
1100	720	4	3	2	15	no	no
1100	720	4	3	2	30	no	no
1100	720	4	3	8	15	yes	no
797	510	2.8	3	4	15	no	no
1268	830	4.6	3	4	15	no	yes

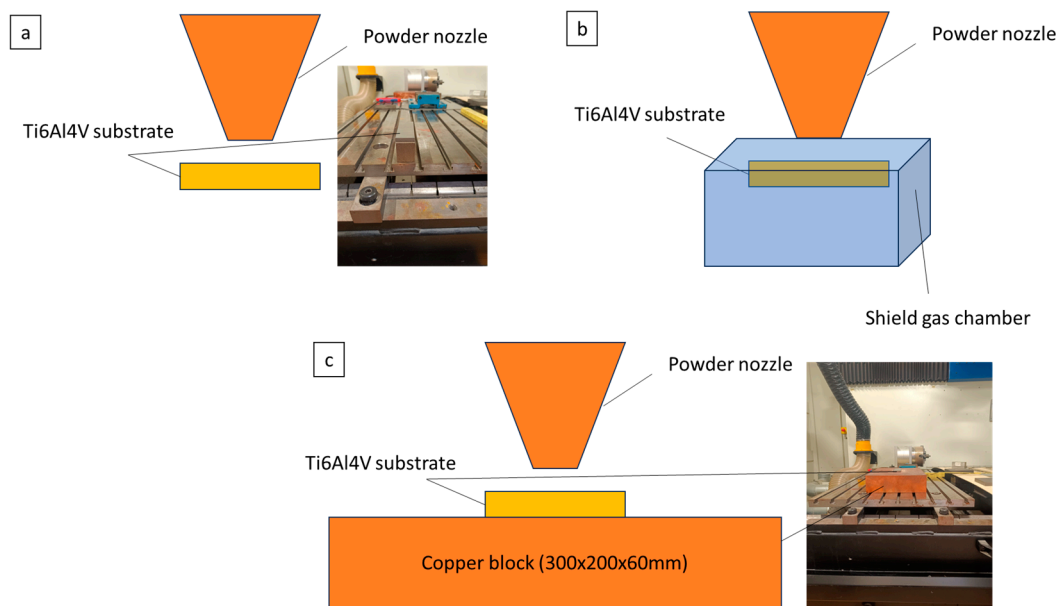


Figure 3. Experimental set-up for the DMD experiments: (a) conventional set-up, (b) with shield gas chamber and (c) with heat sink.

To explore the impact of travel speeds, their values were changed. In order to achieve constant deposit conditions according to the literature, the line energy or specific energy, as per Equations (1) and (2), were kept constant. For this purpose, the laser power was adjusted accordingly, ensuring that the specific energy for all experiments was 30.6 J/mm² and the line energy was 91.7 J/mm. Additionally, the powder deposition mass per unit length, m_p , was kept constant at 5.5 g/m across all experiments, maintaining as consistent deposition conditions as possible. The powder deposition mass was calculated using the following equation:

$$m_p = \frac{\dot{m}}{v}, \tag{6}$$

where \dot{m} represents the mass flow rate in g/min and v denotes the travel speed in mm/min. A schematic representation of the experimental setup for the DMD experiments is depicted in Figure 3.

Twelve singletracks were built next to each other with an overlap of 50%, resulting in one layer. Four layers were built up on top of each other to achieve a sufficient height for the microhardness measurement and the necessary dimensions for the tensile samples.

The Qness Q10 microhardness tester was used to measure the microhardness. To obtain a statistically significant hardness measurement across the substrate and the deposit, three microhardness curves were measured. The measurement scheme can be found in Figure 4.

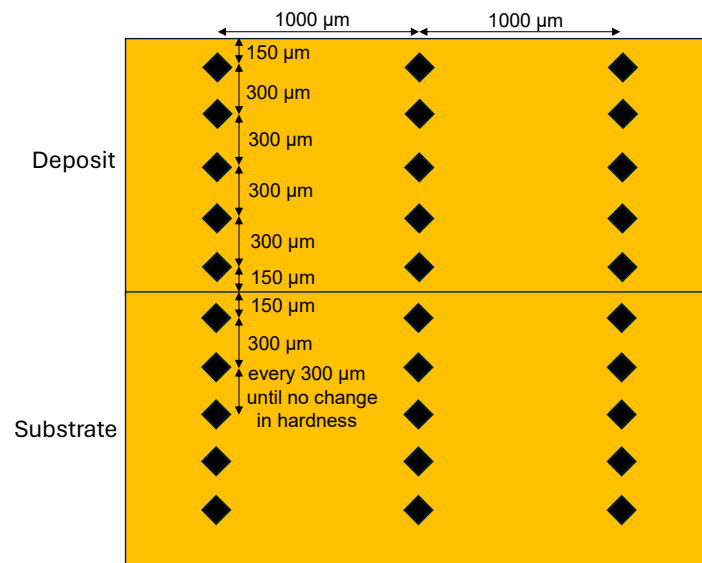


Figure 4. Schematic methodology for conducting a series of microhardness measurements.

The Vickers hardness HV0.3 was measured in accordance with the DIN EN ISO 6507 [24] standard, to enable the determination of a hardness profile with a sufficiently fine resolution. The distance from the specimen edge was 3d and 6d (where d is the length of the impression diagonal) between the individual test points and corresponded to the defined minimum distance of the DIN EN ISO 6507 standard, thus avoiding any influence on the hardness test due to work hardening.

To determine the tensile strength and ductility of the individual Ti6Al4V samples, specimens were cut from the deposit using electrical discharge machining (EDM). In each case, three samples were cut in the build-up direction and three samples at 90° to the build-up direction, to investigate the directional influence of the DMD process. A schematic representation can be found in Figure 5.

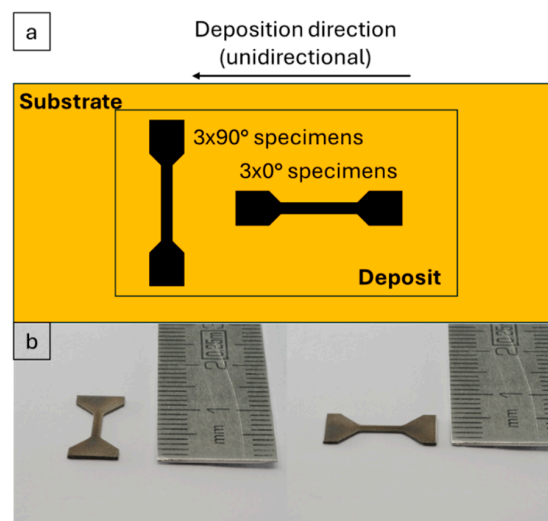


Figure 5. Extraction of micro-tensile specimens through EDM. To determine the directional dependence of the direct metal deposition (DMD) process, samples were machined from the deposit in various orientations. (a) Schematic representation, (b) real specimens.

The width of the individual specimen was 1 mm and the thickness was 0.3 mm. The principle and performance of micro tensile tests were explained, and the suitability of this measurement method for micro tensile specimens was demonstrated, in Beerli et al. [25]. Before measuring the tensile strength, the width of all individual samples was measured using the Keyence VHX-7000 digital microscope to analyse the microstructure, and Kroll etching was used to visualize it. An overview of the methodology described is illustrated in Figure 6.

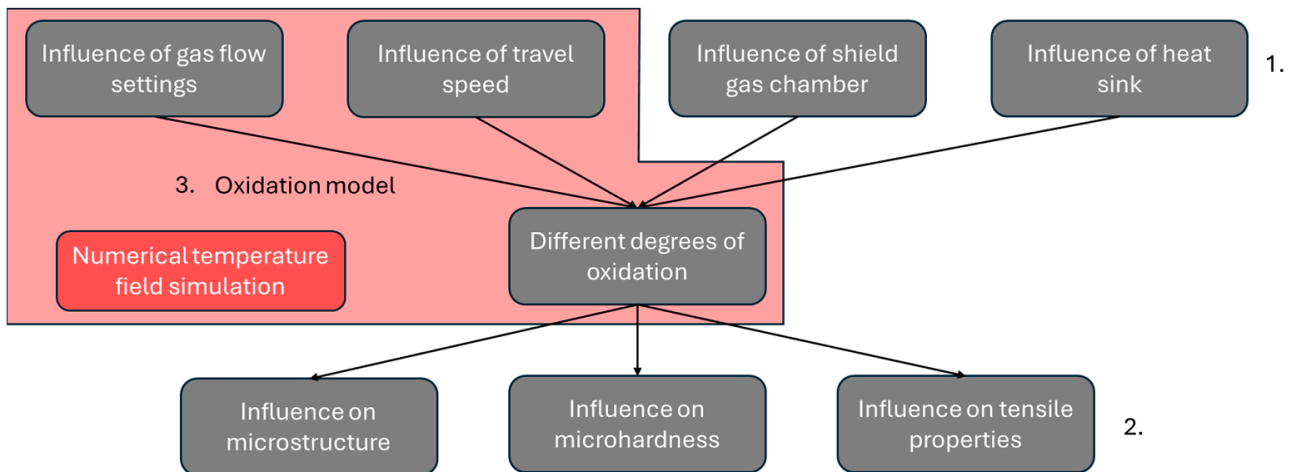


Figure 6. Schematic representation of the methodology. First, the influence of the gas flow settings, travel speed, protective gas chamber and a heat sink on the degree of oxidation was investigated. Based on this, the influence of the degree of oxidation on the microstructure, microhardness and tensile properties was examined. Finally, an oxidation model was developed which, based on a numerical temperature field simulation, showed a way of reducing oxidation.

The numerical model is presented in the next Section.

3. Numerical Simulation

The temperature fields were simulated numerically with the Comsol Multiphysics 6.1 software. Two different models were developed for the calculation of these, differing only in that, in one model, the melt pool flow was considered and, in the other, it was not, in order to achieve a higher computational efficiency, as mentioned in Soffel et al. [26]. Detailed information on the simulation approach is described in Wirth and Wegener [27] and can be taken from there.

3.1. Model Domain

The model domain has a rectangular cross-section with a length of 11 mm, a width of 5 mm and a height of 3 mm. The laser beam is fixed in the model domain at the position $x = 4.5$ mm and $y = 0$ mm and applies its energy to the substrate at $z = 0$ mm. The model domain with the associated coordinate system is shown in Figure 7.

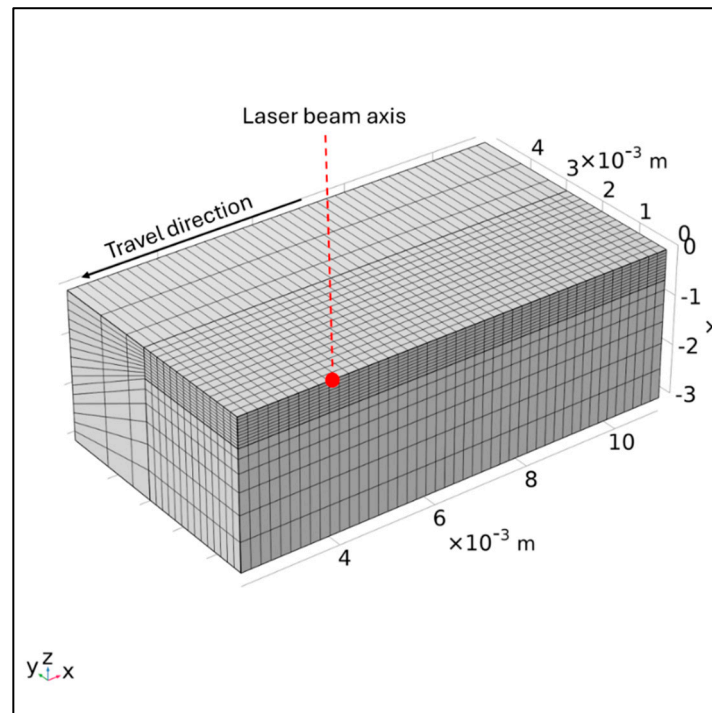


Figure 7. The model domain with fixed beam source for the temperature field calculation.

3.2. Heat Source Definition

The input of laser power is simulated by means of a surface heat source $Q(x, y)$. The heat source can be described as follows:

$$Q(x, y) = I(x, y) \cdot \alpha_{WP} \tag{7}$$

where $I(x, y)$ is the spatial intensity distribution and α_{WP} is the absorption coefficient of the work piece. The spatial intensity distribution $I(x, y)$ can be described as a circular heat source, as follows:

$$I(r) = \frac{2P}{\pi r_L^2} e^{-2\frac{r^2}{r_L^2}} \tag{8}$$

where P is the laser power and r_L is the radius of the laser spot. The assumption is made that the intensity distribution of the laser beam is bivariate Gaussian. The heat source is fixed at the position of $x = 4.5 \text{ mm}$ and $y = 0 \text{ mm}$ in the model domain. The radial distance r can be calculated using the following equation:

$$r(x, y) = \sqrt{(x - 4.5\text{mm})^2 + y^2} \tag{9}$$

A plot of the intensity distribution is shown in Figure 8.

For r_L , 1.5 mm was chosen, as this corresponds to the laser beam radius on the surface of the substrate with which the experiments were carried out.

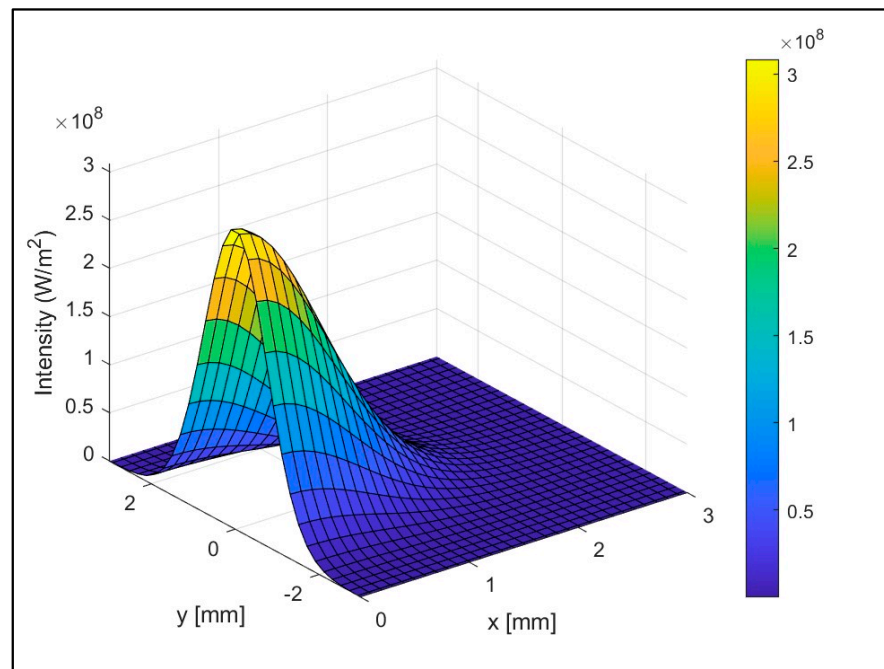


Figure 8. Intensity distribution of the laser beam, defined as a surface heat source.

3.3. Heat Conduction Model

The governing equation is the three-dimensional, simplified heat conduction equation that follows:

$$\rho c_p \frac{\partial T}{\partial t} - \nabla \cdot (k \nabla T) = 0 \tag{10}$$

where ρ is the density, c_p the isobaric heat capacity, k the thermal conductivity of the material, T the temperature and $\frac{\partial T}{\partial t}$ its time derivative. Heat losses due to convective heat transport and thermal radiation are not considered—the former to fulfil the pure heat conduction character and the latter because it has a negligible influence on the melt pool geometry.

3.4. Fluid Flow Model

In the fluid flow model, heat convection within the melt pool flow is considered, and heat loss is taken into account by means of convection. The relevant equations that are solved consist of the continuity equation, as follows:

$$\nabla \cdot \underline{u} = 0 \tag{11}$$

$$\rho c_p \frac{\partial T}{\partial t} + \rho c_p \underline{u} \cdot \nabla T + -\nabla \cdot (k \nabla T) = 0 \tag{12}$$

where \underline{u} is the velocity vector of the fluid flow. The heat conduction equation which describes the convective heat transport, and finally the Navier–Stokes equation for incompressible flows, is given by the following:

$$\rho \left[\frac{\partial \underline{u}}{\partial t} + \underline{u} \cdot (\nabla \otimes \underline{u}) \right] = \nabla \left\{ -p \underline{I} + \mu \left[\nabla \otimes \underline{u} + (\nabla \otimes \underline{u})^T \right] \right\} + \underline{F} \tag{13}$$

where p is the pressure, \underline{I} is the unit tensor and \underline{F} is the volume force vector, via which buoyancy and gravitational effects of the fluid flow are taken into account. However, it should be noted that the melt pool flow and the heat loss due to convection lead to an extension of the computational time of a factor of 60, with negligible changes to the melt pool geometry and the temperature field. This is also described in the work by Soffel et al. [26]. For this reason, only the heat conduction model is considered in Sections 4 and 5. Further-

more, by neglecting the heat loss due to convection in the subsequent oxidation model, a more secure estimate is obtained, as the temperature field is extended by considering heat conduction alone.

3.5. Material Properties

For the specification of the material properties, the literature was analysed for constant and temperature-dependent material properties. The constant material properties used for the simulation of the temperature field of Ti6Al4V during the DMD process can be found in Table 3, and the temperature-dependent material properties can be found in Table 4.

Table 3. Constant material properties of Ti6Al4V for the simulation of the temperature field.

Property	Value
Solidus temperature	1878 K [28,29]
Liquidus temperature	1933 K [28,29]
Latent heat/melting enthalpy	$3.65 \cdot 10^{-5}$ J/kg [30]
Absorptivity	0.34 [31]
Volume expansion coefficient	$8.9 \cdot 10^{-6}$ 1/K [32]
Density	4420 kg/m ³ [32]
Viscosity	$3.2 \cdot 10^{-3}$ kg/m s [33]
Surface tension	1.65 N/m [33]
Surface tension coefficient	$-2.4 \cdot 10^{-4}$ N/m K [33]

Table 4. Temperature-dependent material properties of Ti6Al4V for the simulation of the temperature field. All data are taken from Lu et al. [32].

Temperature [K]	Thermal Conductivity [W/m K]	Heat Capacity at Constant Pressure [J/kgK]
293	7	546
478	8.75	584
773	12.6	651
1268	22.7	753
1373	19.3	641
1473	21	660
1873	25.8	732
1923	83.5	831
2273	83.5	831

The temperature dependence of the surface tension is calculated as follows:

$$\sigma_{St} = 1.65 - 2.4 \cdot 10^{-4}K \tag{14}$$

where the first term is the surface tension from Table 3 and the second term is the product of the surface tension coefficient from Table 3 and the temperature T .

4. Results and Discussion

In a study by Keller et al. [23], the oxygen content was determined in weight percentage using hot carrier gas extraction for the experiments in Table 2. The values are listed in Table 5.

The powder used has an average oxygen content of 565 ppm with a standard deviation of $\sigma_p = 3.13$ ppm, and the Ti6Al4V substrate has an oxygen content of 1160 ppm with a standard deviation of $\sigma_{Sub} = 15.4$ ppm. The influences of the different degrees of oxidation on the microstructure, microhardness and tensile strength are shown in Sections 4.1–4.3.

Table 5. Oxygen concentration within the microstructure of the different build-ups. Four cubes were extracted from each sample to quantify the oxygen concentration.

Experiment	Oxygen Content [ppm]	Standard Deviation [ppm]
1	1320	120
2	1120	95.2
3	4920	533
4	1110	74.8
5	1320	134
6	1230	101
7	1010	21.6
8	874	29.3
9	2240	437

4.1. Microstructure Analysis

Figure 9 shows different grain structures in the deposited material and the substrate.

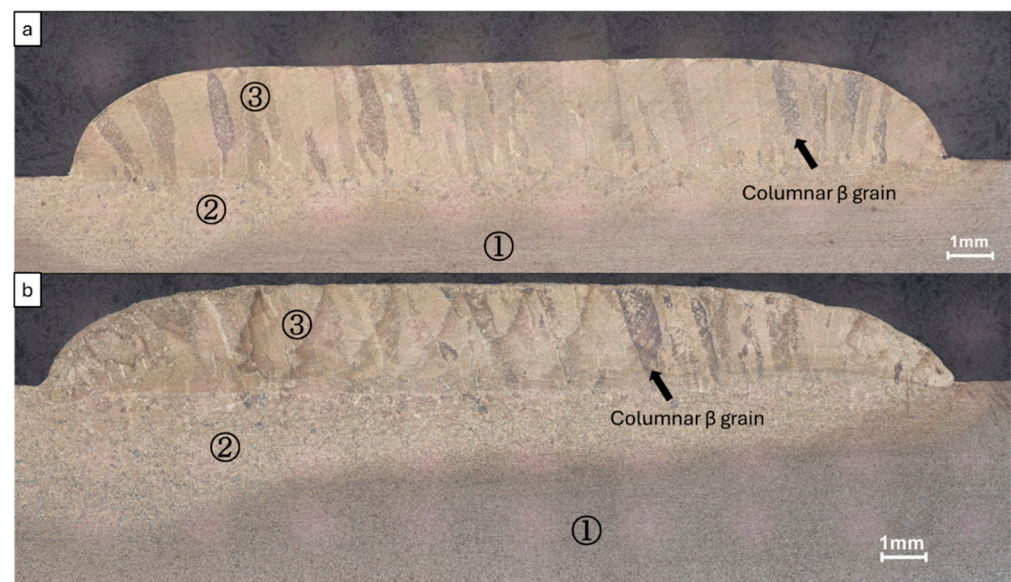


Figure 9. Overview of the microstructure of substrate ①, heat-affected zone (HAZ) ② and build-up ③. (a) Experiment 1 with an oxidation level of 1320 ppm and (b) Experiment 3 with the highest oxidation level of 4920 ppm.

Area ② shows a grain change due to the absorbed laser power and the heat conduction of the hot melt pool towards the deeper substrate material, area ③ shows columnar growth of β grains and area ① shows the grain structure of the thermally unaffected substrate area. The macroscopic structure of DMD-deposited Ti6Al4V is characterized by the epitaxial growth of substantial columnar prior β -grains, extending consistently across the deposited layers. This subdivision of the microstructure into three parts appears to be independent of the degree of oxidation. In order to gain a more precise insight into the microstructure, detailed images of the individual areas were taken. These can be seen in Figure 10.

Figure 10b shows an α -Widmanstätten structure in higher layers of the build-up. The columnar grain growth in the build-up results from the high temperature gradients present in additive processes, which allow directional solidification over the height. The presence of the α -Widmanstätten structure can be explained by the complex thermal history of the DMD process. With increasing layer height, heat accumulates and the temperature gradient, G , decreases [34]. As a result, the ratio G/R (R describes the solidification rate), which is decisive for the morphology of the microstructure, decreases. As the ratio of G/R decreases, diffusion-driven processes are increasingly present, leading to the formation of the α -Widmanstätten structure. This is in agreement with the statements of

Fan et al. [35], who reported α -Widmanstätten structures when the cooling rate fell below 410 K/s. Figure 10c shows a completely different characteristic of the microstructure in the HAZ. This zone experiences a rapid cooling rate at the beginning of the DMD process. This results in the formation of an α' (martensite) microstructure, which is characterised by diffusionless folding. The microstructure of the thermally untreated substrate can be seen in Figure 10d. This zone shows α equiaxed, α elongated grains, β equiaxed and β elongated grains and results from the combined production process using rolling and subsequent annealing. The rolling process leads to elongated grains, whereas the annealing process leads to recrystallisation, resulting in equiaxed grains. There is no change in the microstructure when the same laser power and travel speeds and spot diameters are used (experiments 1–7). This shows that the degree of oxidation has no influence on the microstructure, as experiment 3 shows a significantly higher oxidation, but the formation of the microstructure results solely from the thermal history (e.g., G/R ratio).

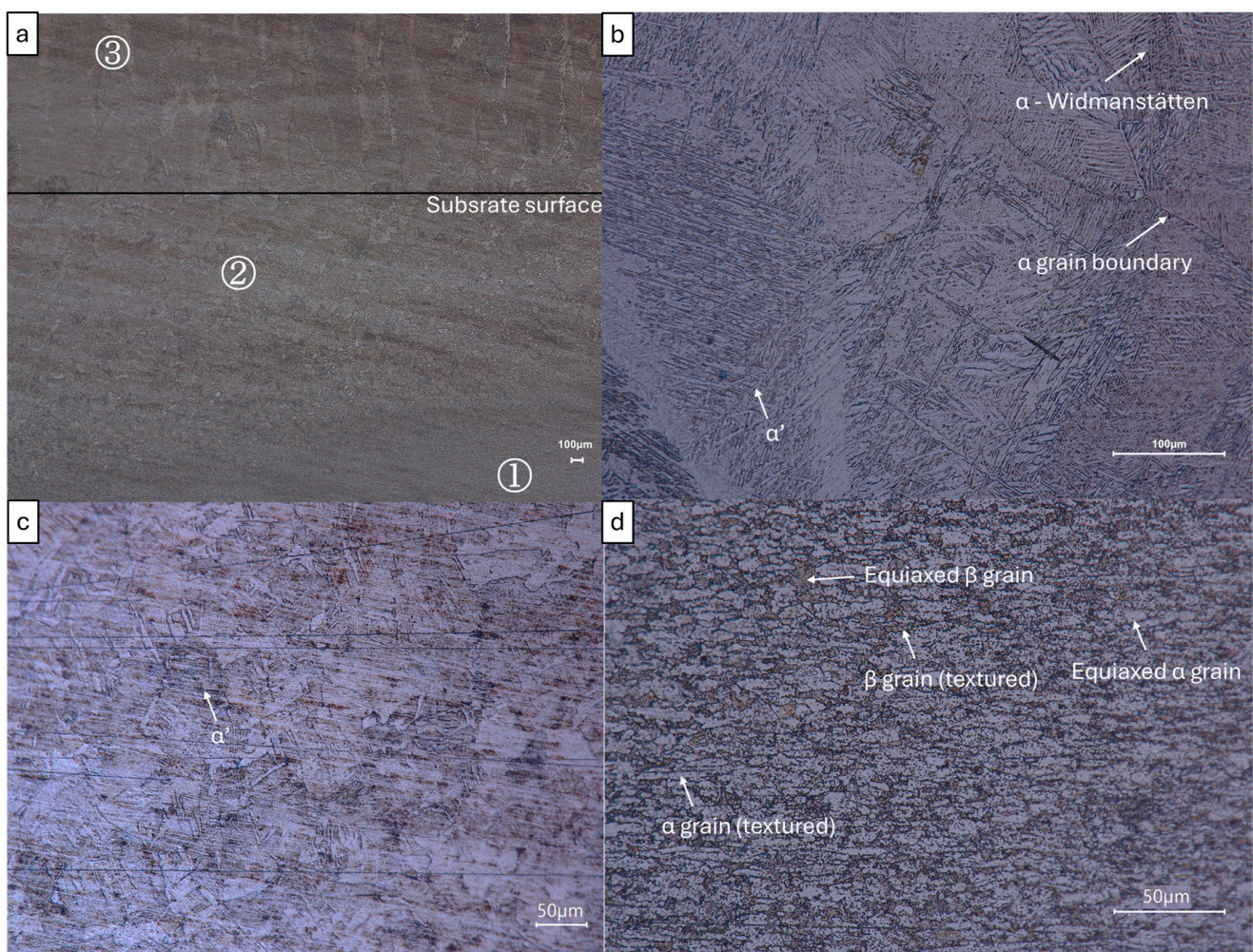


Figure 10. Detailed images of the individual microstructure areas of experiment 1. (a) Zone ① shows the substrate thermally unaffected by the DMD process, zone ② shows the heat-treated area in the substrate with equiaxed grains and zone ③ shows the DED build-up with columnar grain growth, (b) microstructure of the build-up, (c) microstructure of the HAZ, (d) microstructure of the substrate.

4.2. Microhardness Analysis

Figure 11 shows the result of the microhardness measurement of the individual experiments.

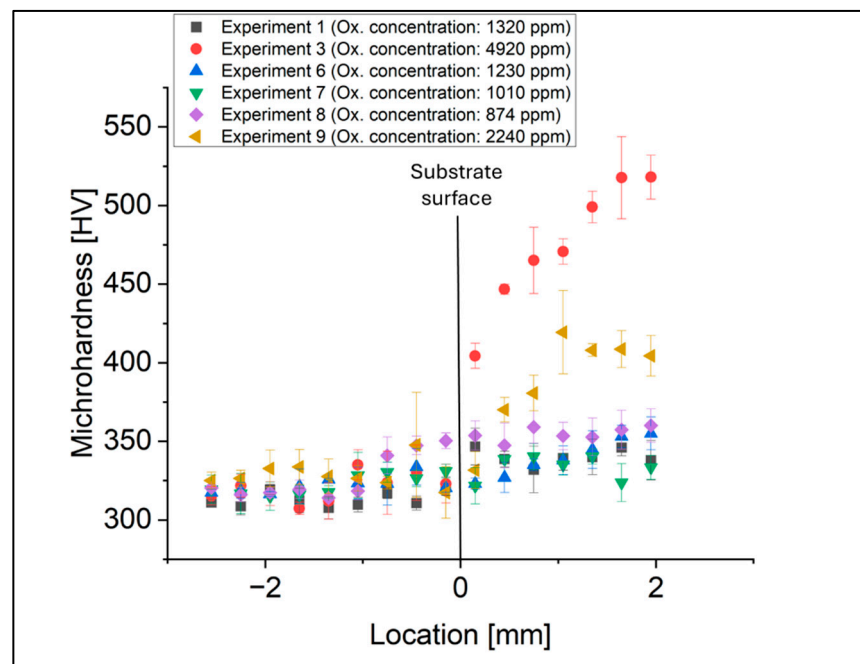


Figure 11. Microhardness measurement of the individual experiments with different oxygen contents.

The location is specified on the x -axis, where zero is the substrate level, values $< zero$ are measured values in the substrate and, therefore, values $> zero$ are hardness measurement points in the build-up area. The microhardness shows a clear difference between the individual experiments with different oxidation rates in the build-up material. Since the microstructure is independent of the degree of oxidation, as described in Section 4.1, it can be concluded that the increase in hardness in the build-up can be explained primarily by the different degree of oxidation. This change in hardness applies in substrate areas close to the surface ($<150 \mu\text{m}$) and in the build-up area. However, the difference in hardness cannot be explained by the oxygen content in the microstructure alone. For example, experiment no. 8 shows higher hardness values than the more oxidised experiments 1, 6 and 7. This means that there must be another hardness increase mechanism that cannot be described by the oxygen content alone. Solidification or precipitation hardening is unlikely, as neither deformation took place nor was an additional phase recognisable in the microstructure. The increase in hardness could therefore be caused by solid solution hardening and, thus, by dissolved, hardness-increasing elements. In addition to the diffused oxygen, the two elements nitrogen and hydrogen are also present. Above all, the increase in hardness in areas close to the surface (x almost 2 mm) through the diffusion of hydrogen into the titanium microstructure due to its small atomic radius appears logical. A stable formation of a surface rutile layer would act as an inhibitor for the diffusion of hydrogen [11]. However, as this does not show any real adhesion at temperatures $>700 \text{ }^\circ\text{C}$ and these temperatures are exceeded with DMD, the assumption of hydrogenation of the microstructure, which leads to an increase in hardness, is logical. Hydrogenation can also be used to explain the hardening in substrate areas close to the surface ($<150 \mu\text{m}$). Due to the slower process of experiment 8 (travel speed of 510 mm/min instead of 720 mm/min compared to experiments 1, 3, 6 and 7), the diffusion of hydrogen through the ambient atmosphere inside the substrate can take place over a longer period of time. This can explain the onset of hardness of the experiment 8 of approximately 30 HV at the location $x = -150 \mu\text{m}$. This explanation can be supported by the lowest hardness values measured in the build-up areas near the surface ($\leq 2 \text{ mm}$) of experiment 7. This experiment was carried out inside a shielding gas chamber and the hardening of the edge area by diffusion of hydrogen or nitrogen cannot take place or can only take place to a small extent. As a result, no hardening takes place here and experiment 7 shows the lowest hardness values for build-up areas

near the surface. However, a longer diffusion time (see above explanation of the increase in hardness of experiment 8) cannot explain the increase in hardness of experiments 3 and 9, as experiment 3 was carried out at the same travel speed as experiments 1, 6 and 7 and experiment 9 was even at an increased travel speed. The increase in hardness in experiments 3 and 9 can therefore be explained purely by solid solution hardening due to diffusing oxygen and the formation of the oxygen-enriched solid solution (referred to in the literature as the α case [28]). In experiment 3, the α case forms due to unfavourable process parameters with regard to the carrier to shield gas volume flow ratios. By exceeding a ratio value of 0.3 in this case, a sufficient shielding gas atmosphere is not formed according to the work of Keller et al. [22]. In experiment 9, solid solution hardening by oxygen occurs due to an unfavourable temperature field with regard to the spatial oxygen concentration present. A detailed explanation can be found in Section 4.4.

4.3. Tensile Tests

Figure 12 shows the stress–strain diagram of experiments 1, 3 and 4.

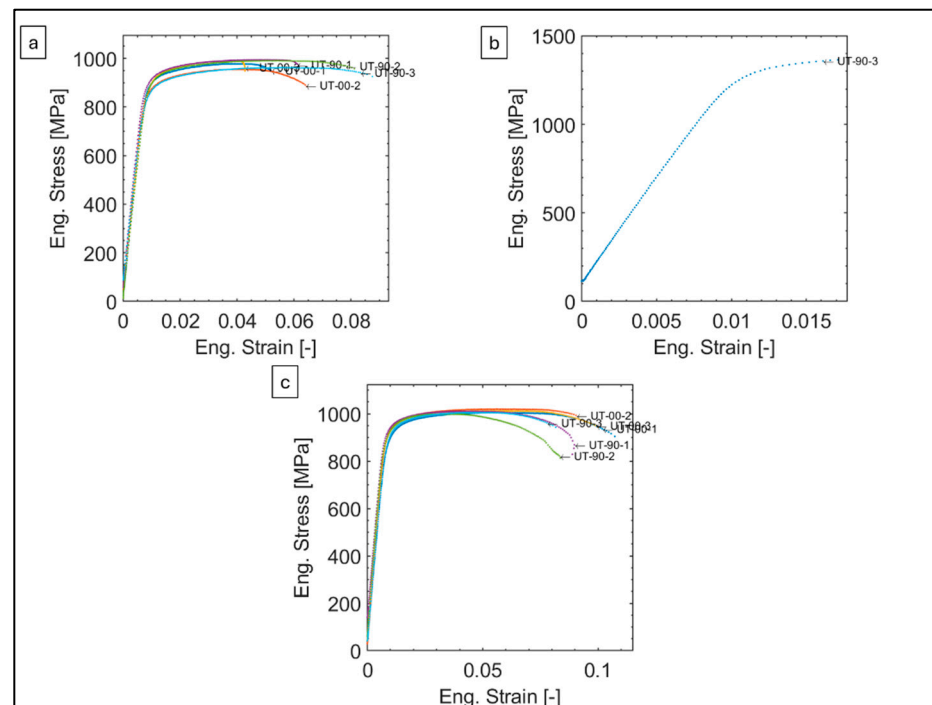


Figure 12. Stress–strain curves for different experiments. (a) Experiment 1, (b) experiment 3 and (c) experiment 4. The engineering stress and the engineering strain could be determined for only one of six tensile tests, as the remaining five tensile specimens of experiment 3 did not show any plastic behaviour and, therefore, it was not possible to create the diagram.

As can be seen from Figure 12, experiment 1 and experiment 4 show a significantly different stress–strain curve compared to experiment 3. This can be explained by the very different degree of oxidation (experiment 1 has a degree of oxidation of 1320 ppm, experiment 3 of 4920 ppm and experiment 4 of 1110 ppm). Experiment 3 in Figure 12b shows a strong embrittlement due to the high oxidation, which leads to an increased ultimate tensile strength (UTS) with strongly reduced ductility. This is also shown by the lack of necking in experiment 3 when performing the tensile test, as can be seen in Figure 13.

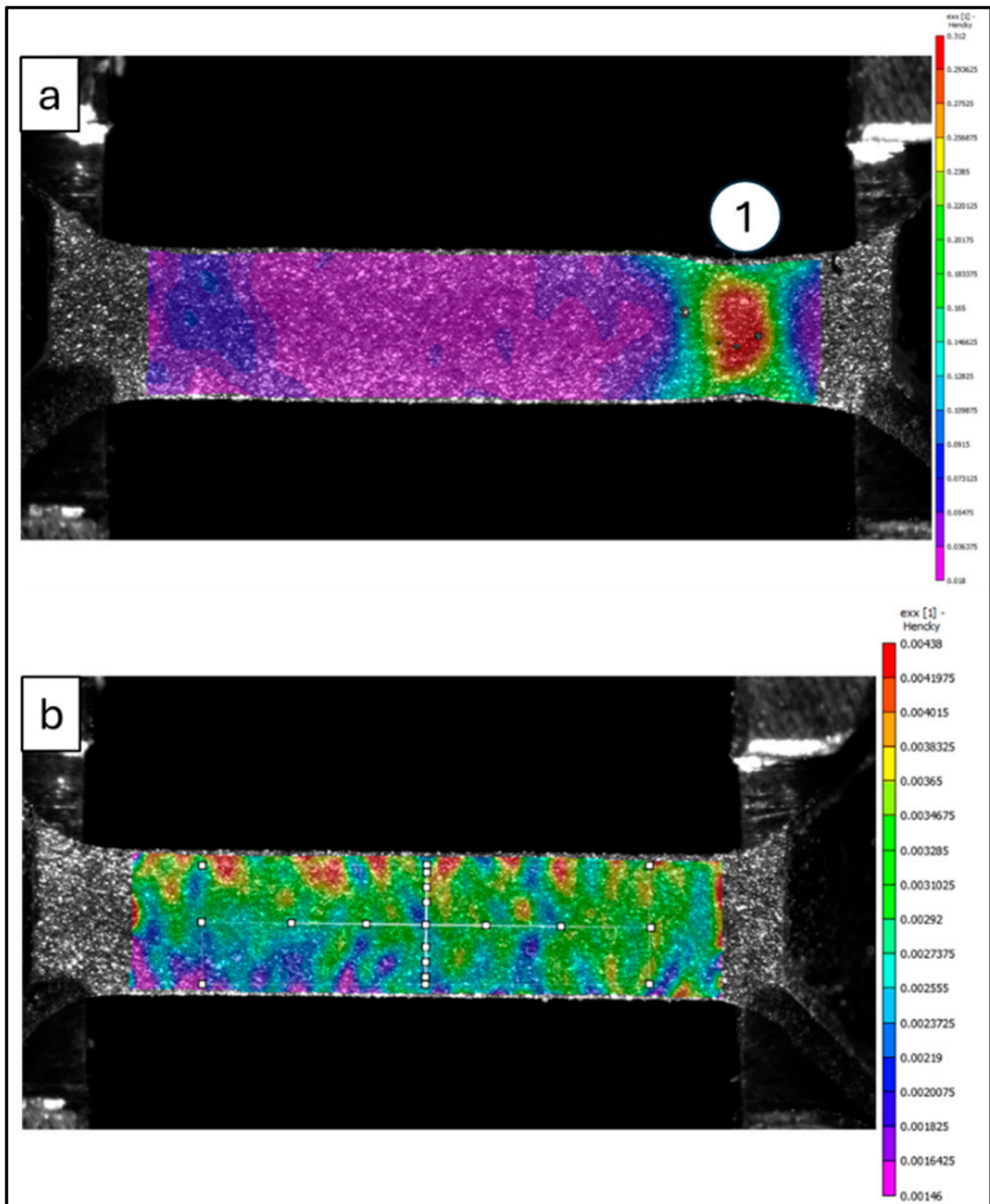


Figure 13. True strain map for various experiments. (a) Experiment 1 and (b) experiment 3. Experiment 1 shows a present necking ①, whereas experiment 3 does not and is a sign of a brittle fracture.

Figure 12a,c shows a UTS > 920 MPa and an elongation at failure of >5%. Experiment 4 shows higher values of elongation at failure compared to experiment 1. This can also be explained by the lower degree of oxidation in experiment 4 compared to experiment 1. No uniform statement can be made regarding the orientation of the test sample regarding the

build direction. For example, there is no difference between the sample orientation and the UTS. No clear tendency can be determined based on the elongation either. Experiment 1 shows a greater elongation at failure in the 90° direction, whereas experiment 4 shows a reduced elongation at failure in the 90° direction compared to the 0° direction. This study closes the knowledge gap that was not analysed by Bambach et al. [36], who investigated the tensile properties parallel and perpendicular to the build-up direction in a thin-walled structure, meaning that characterisation perpendicular to the build-up of a layer (in the present study: 90° orientation) could not be investigated. It can, therefore, be concluded that the sample orientation, as defined in this paper in Figure 5, plays a negligible role.

Finally, the tensile properties must be compared with the requirements defined in standards. For Ti6Al4V components, these are defined in the standards DIN 17,864 (for forged parts) and DIN 17,865 (for cast parts). The comparison of the values is shown in Table 6.

Table 6. Comparison of oxygen content, yield strength, tensile strength and elongation at failure for samples with different oxygen contents.

Experiment	Oxygen Content [ppm]	Yield Strength, YS [MPa]	Tensile Strength, UTS [MPa]	Elongation at Failure, [%]
1	1320	859 ± 9.5	952 ± 20.1	6 ± 0.5
2	1120	842 ± 6.2	922 ± 15.7	7 ± 0.6
3	4920	1267	1370	1.5
4	1110	839 ± 7.2	915 ± 16.9	7 ± 0.4
5	1320	836 ± 6.2	921 ± 17.1	6 ± 0.7
6	1230	865 ± 11.7	968 ± 19.4	8 ± 0.6
7	950	862 ± 15.5	952 ± 30.5	11 ± 0.8
8	874	840 ± 12.1	958 ± 22.3	3 ± 0.8
9	2240	862 ± 21.5	969 ± 40.3	5 ± 0.8
Cast DIN 17,865	-	≥785	≥880	≥5
Forged DIN 17,864	-	≥830	≥900	≥10

As can be seen from Table 6, experiments 1, 2, 4, 5, 6 and 7 fully meet the requirements regarding yield strength (YS), UTS and elongation at failure, in accordance with DIN 17,865. In comparison to the requirements for forged parts, this only applies to the YS and UTS, but the experiments show insufficient ductility. Experiment 7 is the only experiment that also fulfils all the requirements of DIN 17,865. The reason for this is that this experiment was set up inside a shielding gas chamber and thus, in addition to a low oxygen content, less nitrogen and hydrogen can diffuse into the microstructure, which has a positive effect on the ductility of this sample. Experiment 3 shows strong embrittlement due to its high oxygen content. This is reflected in the high YS and UTS, but the elongation at failure is insufficient. Experiment 8 shows sufficient strength properties at low oxygen content, but with insufficient elongation at failure. The cause of this phenomenon lies in the presence of porosity or insufficient fusion, as evidenced by microscopy images. This condition restricts the ductility observed in this experiment. Although this experiment was set up with constant specific energy and powder section mass, as mentioned in Section 2, the application conditions change. The numerical simulation, the results of which are described below, should provide clarity on this. Experiment 9 fulfils the requirements of DIN 17,864 and DIN 17,865 with regard to YS and UTS, but the elongation at failure cannot be met with sufficient certainty, due to embrittlement caused by the excessive degree of oxidation.

In general, these experiments show the high potential of DMD for the production of components. For example, without a shielding gas chamber (experiments 1, 2, 4, 5 and 6), Bambach et al. achieved similar or in some cases better values for the elongation at failure of the wire arc manufacturing experiments, which were carried out inside a shield gas chamber [36]. Experiments 1, 2, 4, 5 and 6 thus show a superposition of the temperature field with the spatial oxygen concentration, which makes the DMD process non-critical for oxidation. This is described in more detail in Sections 4.4 and 4.5.

4.4. Numerical Simulation

Figure 14 illustrates the results of the numerical simulation for calculating the temperature field.

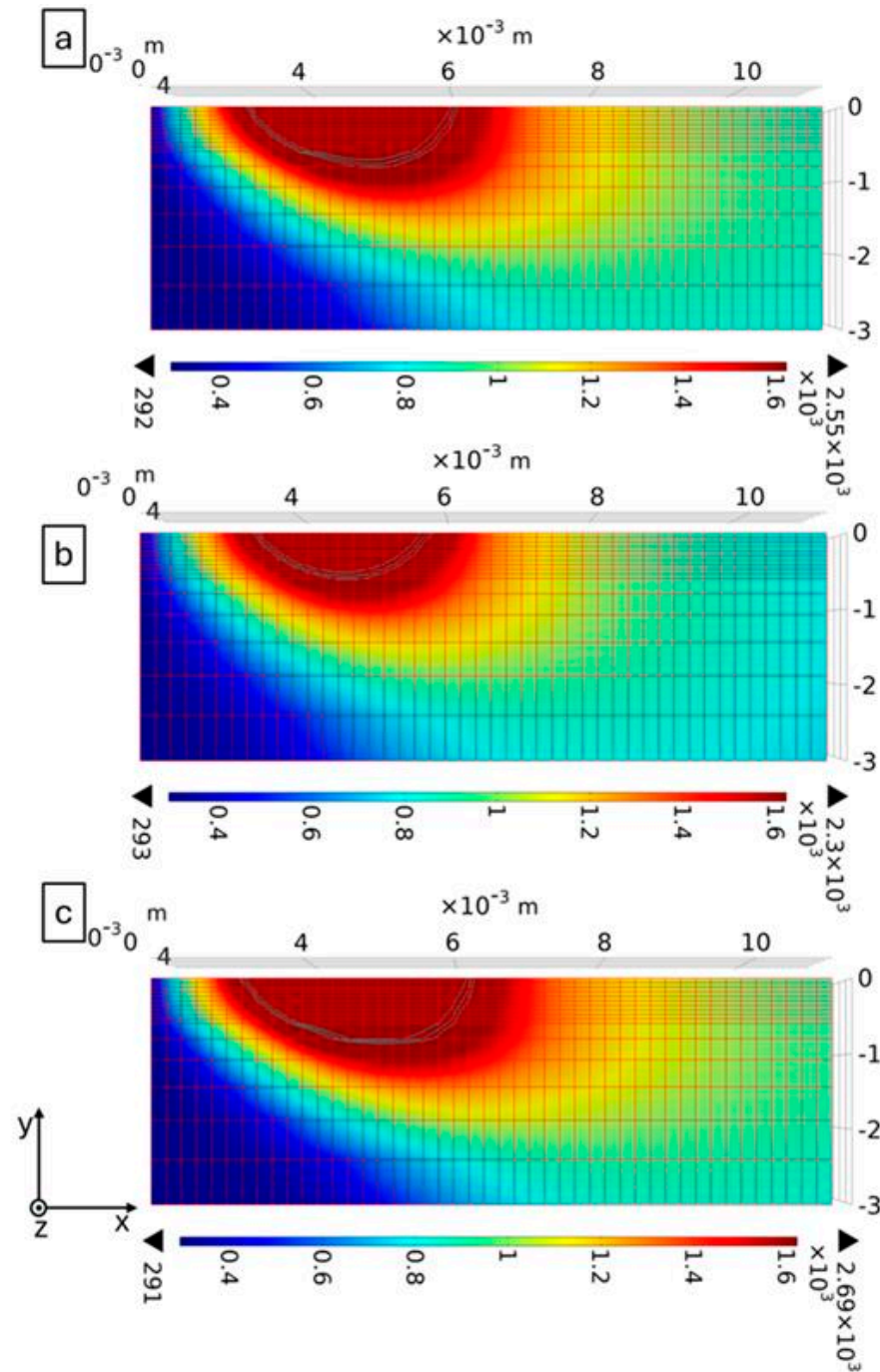


Figure 14. Numerical results of the transient simulation of the temperature fields as a result of heat conduction. All experiments were carried out with constant specific energy and a laser spot diameter of 3 mm. The laser power and travel speed were varied as follows: (a) laser power: 1100 W, travel speed: 720 mm/min, (b) laser power: 797 W, travel speed 510 mm/min and (c) laser power: 1268 W, travel speed 830 mm/min.

Figure 14 demonstrates that at constant specific energy, the results differ greatly. This indicates that the specification of the specific energy alone, as is usual in the literature, is not completely sufficient. At constant specific energy, Figure 14b shows a clear difference

in the spatial expansion of the temperature field compared to Figure 14c. The slower travel speed increases the time it takes for the substrate material to dissipate heat from the hot melt pool region via its thermal diffusivity. With a reduced travel speed, this results in smaller melt pool dimensions and a smaller temperature field.

A higher travel speed leads to an extension of the temperature distributions of the hot, oxidation-critical temperatures above 700 °C for Ti alloys and to increasing overheating with each additional track applied. To create an oxidation model, the lateral dimension in the drawing plane (minus z-direction) of Figure 14 must also be taken into account in a subsequent step. This is shown in Figure 15, which illustrates that the lateral expansion in the minus z-direction of the hot temperatures is significantly lower than in the trailing temperature field in x direction. This means that the expansion of the temperature field in the z-direction is less critical for oxidation.

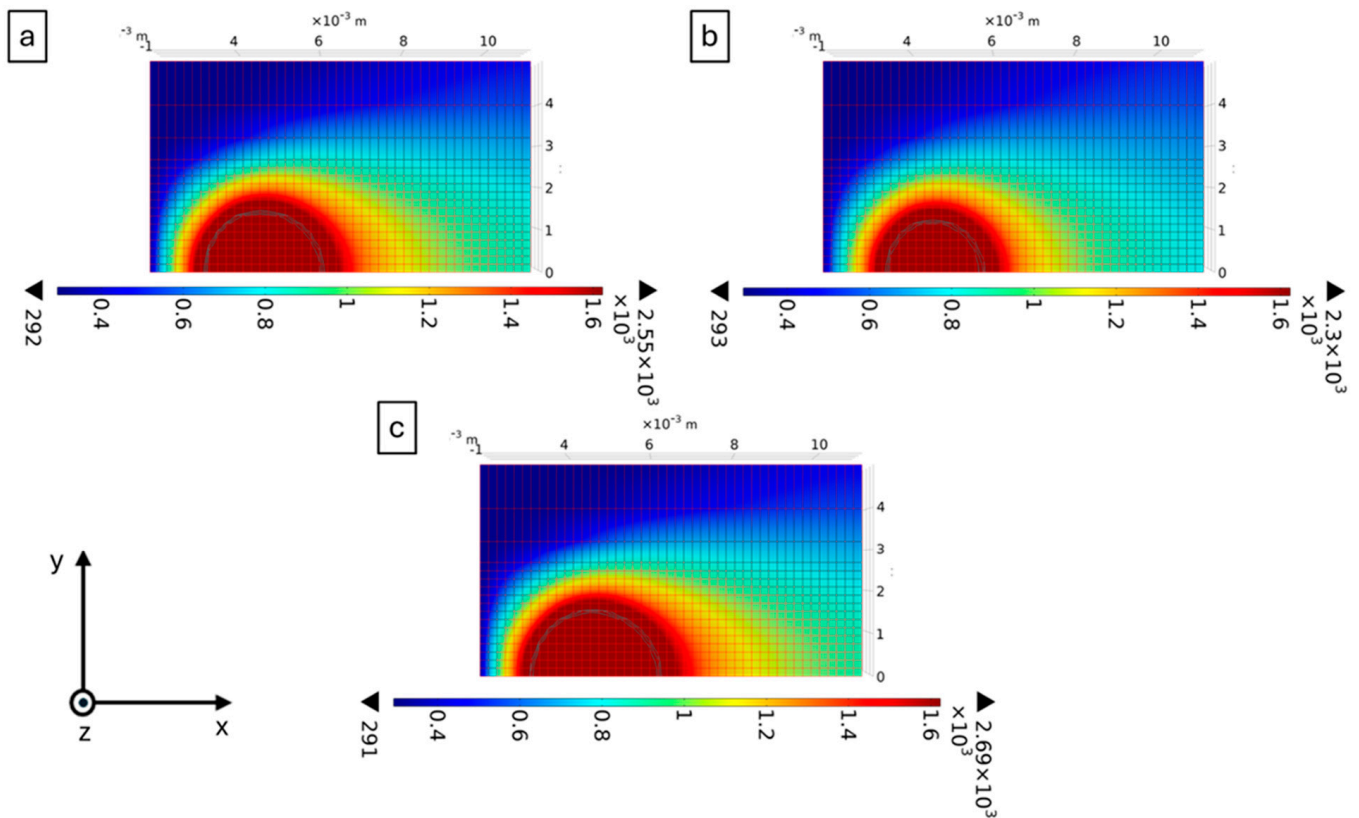


Figure 15. Numerical results of the transient simulation of the temperature fields (top view). All experiments were carried out with constant specific energy and a laser spot diameter of 3 mm. The laser power and travel speed were varied as follows: (a) laser power: 1100 W, travel speed: 720 mm/min, (b) laser power: 797 W, travel speed 510 mm/min and (c) laser power: 1268 W, travel speed 830 mm/min.

4.5. Oxidation Model

4.5.1. Sources of Oxidation

The possible sources of oxygen in the DMD process are summarised in Figure 16 and are taken into account in the model.

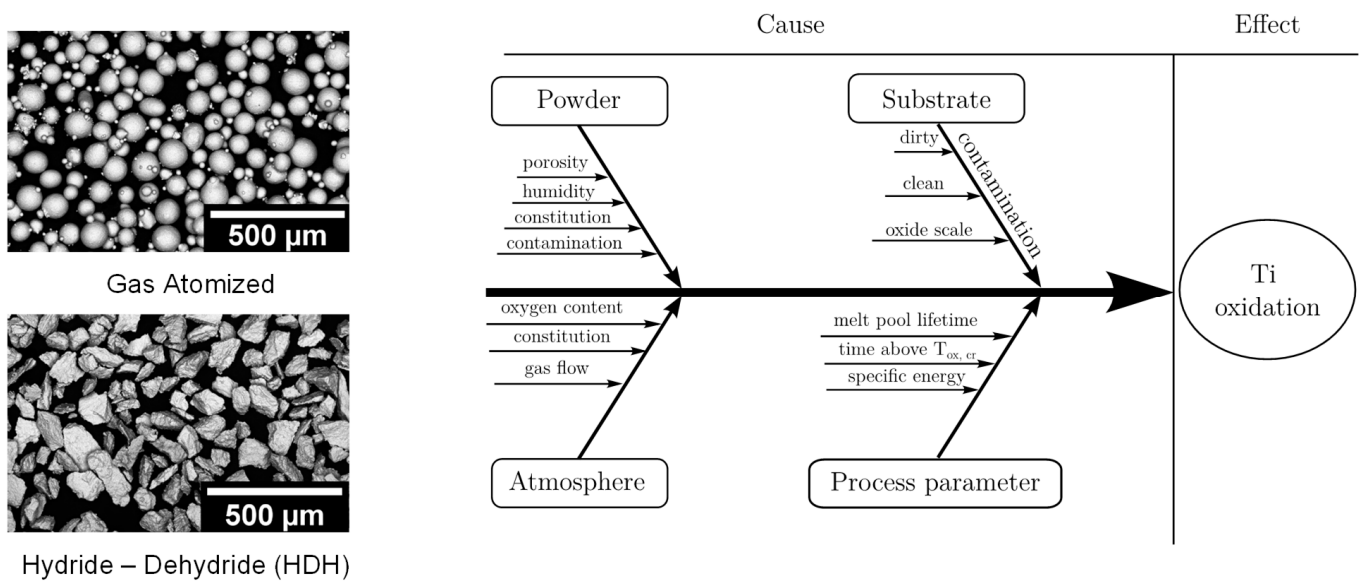


Figure 16. Oxidation sources of the DMD process. The oxidation sources in the Ishikawa diagram summarise the causes for the oxidation (effect) of Ti6Al4V during the DMD process. The powder has a different structure depending on the powder production process, as can be seen in the SEM images on the left.

Figure 16 divides the sources of oxidation into the following four possible main causes:

- The powder: The powder has a different degree of oxidation depending on the manufacturing process. With an equivalent diameter, a spherical shape has the lowest surface energy. This leads to a reduced surface area and thus to a reduced oxide layer on the powder compared to the blocky powder, whose structure is based on the hydride–dehydride (HDH) process. Hot carrier gas extraction measurements showed a degree of oxidation that was increased by a factor of two. The spherical powder produced by the gas atomisation process used in this work has an oxygen content of 500 ppm, whereas the HDH powder has an oxygen content of 1000 ppm.
- The substrate: The substrate may have some contamination in the form of an oxide layer on its surface. For titanium, this oxide layer forms at room temperature. Optical measurements have shown that, at room temperature, the oxide layer thickness is 17 Å after 2 h, around 35 Å after 40 days, 50 Å after 70 days, 75 Å after 545 days and around 250 Å after 4 years [37–40]. Up to about 800 °C, the oxide layer consists exclusively of TiO₂ with a rutile structure, whereby the titanium is enriched with oxygen at the titanium/oxide phase boundary [41–43] and follows a curve according to Equation (4). Above 800 °C, an additional formation of TiO and Ti₂O₃ is observed in [44,45]. However, the proportions of the individual phases were not specified there in more detail. These depend primarily on the rate of formation, i.e., on the disordered structure of the phases and the diffusion rate of the oxygen atoms through the oxide layer [46]. For the following calculation of the amount of oxygen that can be dissolved from the oxide layer, a complete TiO₂ composition of the oxide layer is assumed. Assuming a thickness of the substrate oxide layer of 75 Å and the lateral oxide layer dimensions of 18 mm width and 60 mm length (which corresponds to the coating area during the DMD experiments), this results in an oxide volume of 0.081 mm³. Using the density of rutile of 4.28 g/cm³ [47] results in an oxide layer mass of 3.47·10^{−4} g. The weight fraction of oxygen in rutile totals, from the ratio of the molar masses of oxygen (32 g/mol) to titanium dioxide (79.9 g/mol) [48], approximately 0.4, resulting in a mass that can be extracted from the oxide layer of 1.38·10^{−4} g. An average build-up volume, which is available for dissolving the calculated oxygen mass results from the coating area and the layer height of 3 mm to a volume of 3240 mm³. With the density

Ti6Al4V according to Table 4, the mass of the build-up is 14.6 g. This means that the oxygen contained in the oxide layer could increase the weight proportion of oxygen in the build-up material by around $1.38 \cdot 10^{-4} \text{ g} / 14.6 \text{ g} = 9.45 \cdot 10^{-6} \text{ wt.}\% = 0.095 \text{ ppm}$. This means that the proportion of oxidation due to the dissolution of oxygen in the oxide layer is negligible.

- The atmosphere: As shown in the studies by Keller et al. [22,23], a shielding gas atmosphere against oxidation is only given with sufficient certainty at a carrier gas volume flow to shield gas volume flow ratio of <0.2 . According to Keller et al. [22], this shows a spatial extension of the inert gas bell of around 10 mm in diameter, regardless of the nozzle type. This diameter is used in the following oxidation model.
- The process parameters: The process parameters influence the temperature field. This means that higher specific energies, according to Equation (2), result in an energy input into the material (neglecting attenuation). This is a common assumption for conventional laser cladding, as almost all of the laser energy is absorbed by the substrate. This also tends to increase the temperature field in the substrate, making the process more oxidation-critical. For this reason, the subsequent oxidation model provides sufficient certainty, as the temperature fields, according to Figure 14, were calculated without attenuation by the powder. As described in the introduction to this study, the temperature of $700 \text{ }^\circ\text{C}$ or 973 K is used as the critical oxidation temperature, as, above this temperature, no protective oxide layer adheres to the substrate and the transition from parabolic to linear oxidation behaviour occurs for Ti6Al4V.

4.5.2. Temperature Field Evolution

As can be seen from the above considerations, in addition to the use of a powder with a low oxygen content, the generation of a suitable shielding gas atmosphere with the superposition of a matching temperature field is of crucial importance for an oxidation-uncritical process. A suitable atmosphere can be achieved by maintaining a carrier gas volume flow to shield gas volume flow ratio of <0.2 as measured in [22]. The temperature field must be designed in such a way that the oxidation-critical temperature of the respective material (for titanium alloys this is $700 \text{ }^\circ\text{C}$) lies within the inert gas bell. For the measurements of the three-jet nozzle and the coaxial nozzle, this oxygen gradient is approximately 5 mm from the centre of the nozzle [22]. This means that the diameter of the inert gas bell is approximately 8 mm. If the oxidation-critical temperature is located outside the inert gas bell or in the area of the sharp oxygen gradient, the oxygen concentration rises rapidly. Measurements have shown an oxygen concentration of 1000 ppm at a distance of 5.5 mm from the centre of the nozzle and, 8 mm from the nozzle, the oxygen concentration is already 14,500 ppm [22].

The simulated temperature field, as shown in Figure 14, must now be superimposed with the spatial oxygen concentration. A superposition of the temperature field with the spatial oxygen concentration is shown in Figure 17.

Figure 17 indicates that the temperature fields of the experiments with 1100 W and 720 mm/min travel speed and 797 W and 510 mm/min are not oxidation-critical, as the critical oxidation temperature of $700 \text{ }^\circ\text{C}$ for Ti6Al4V lies within the inert gas bell in these experiments (Figure 17a,b). In contrast, in the experiment with 1268 W and 830 mm/min, the critical oxidation temperature is outside the inert gas bell and the material oxidises strongly (4100 ppm without heat sink and 2240 ppm with heat sink, as described in Section 2). In contrast, the experiments in Figure 17a,b show an oxygen content of 1320 ppm and 874 ppm. This demonstrates the validity of the assumption of a critical oxidation temperature of $700 \text{ }^\circ\text{C}$, which, together with the spatial specification of the oxygen gradient, results in a simple, geometric oxidation model. If the mathematical relationship below is not met, the process is not critical for oxidation.

$$r_{igb} > r_{Tox,cr} \quad (15)$$

r_{igb} is the radius of the inert gas and $r_{Tox,cr}$ is the radius of the critical oxidation temperature (in each case related to the centre of the nozzle or the centre of the laser beam).

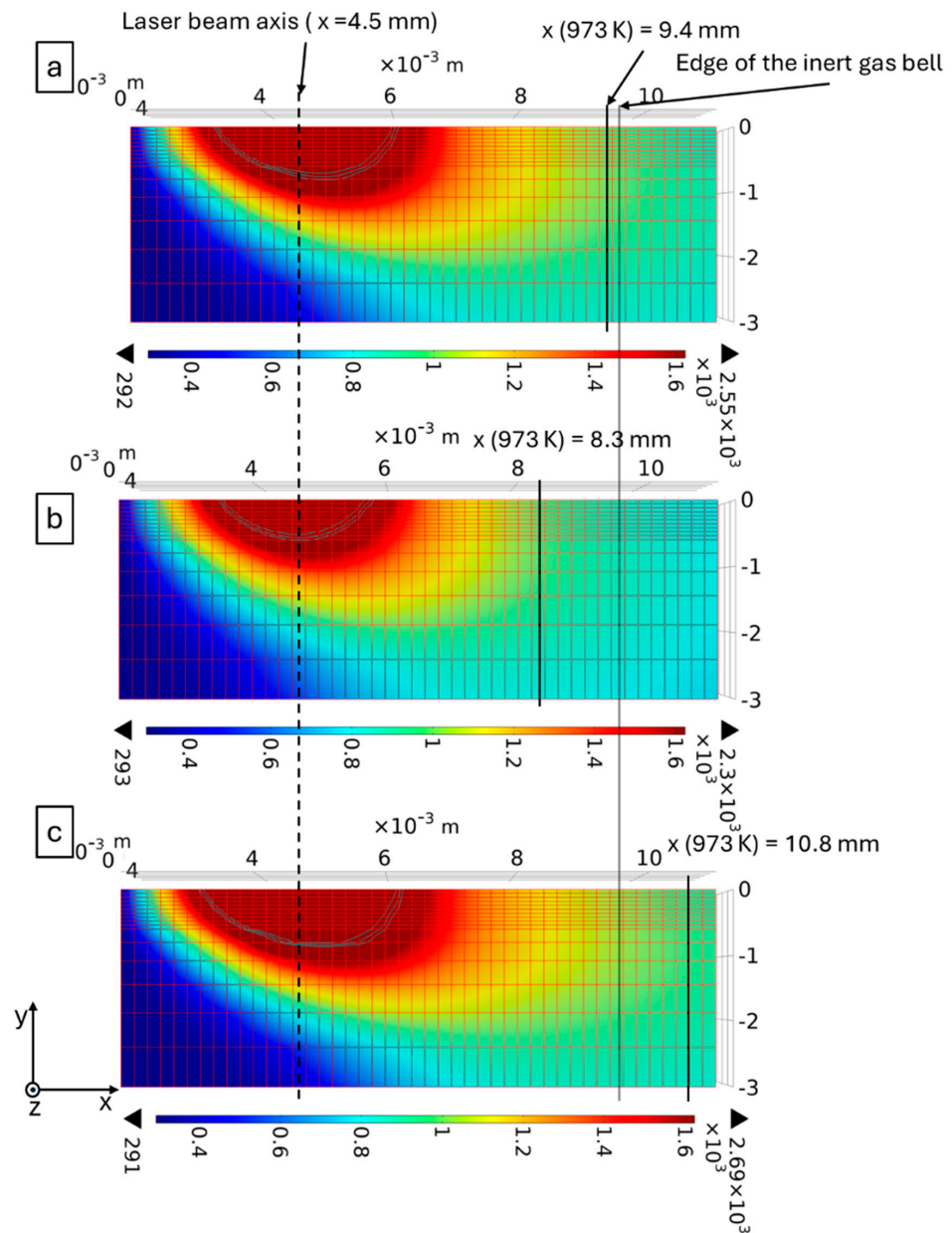


Figure 17. Superposition of the inert gas bell with the temperature distribution. All experiments were carried out with constant specific energy and a laser spot diameter of 3 mm. The laser power and travel speed were varied: (a) laser power: 1100 W, travel speed: 720 mm/min, (b) laser power: 797 W, travel speed 510 mm/min and (c) laser power: 1268 W, travel speed 830 mm/min.

To describe the temperature distribution $T(x, t)$ in the x-direction, the heat conduction equation below has to be solved:

$$\frac{\partial T}{\partial t} = \alpha \nabla^2 T \tag{16}$$

where α is the thermal diffusivity of the substrate material. As can be seen from Figure 17, the temperature distribution in the x-direction is critical for oxidation in the opposite

direction to the travel speed. This simplifies the heat conduction equation in the x-direction to the one-dimensional form of the following:

$$\frac{\partial T}{\partial t} = \alpha \frac{\partial^2 T}{\partial x^2}. \tag{17}$$

The intensity distribution of the laser is proportional to the energy applied to the surface of the substrate. Therefore, the power of the laser over a surface can be used as the source term in the heat conduction equation. The power absorbed by the substrate is as follows:

$$P(x) = \alpha_{WP} \cdot I(x) \cdot A = \alpha_{WP} \cdot I_0 e^{-\frac{x^2}{r_L^2}} \cdot A, \tag{18}$$

where A is the cross-sectional area of the laser focus. This gives the heat input Q per volume, as follows:

$$Q(x) = \frac{P(x)}{A} = I(x). \tag{19}$$

$$\frac{\partial T}{\partial t} = \alpha \frac{\partial^2 T}{\partial x^2} + I_0 e^{-\frac{x^2}{r_L^2}} \tag{20}$$

This is used as the source term in the heat conduction equation and the result is given above (Equation (20)).

Taking into account the constant travel speed v , the heat conduction equation to be solved to determine $T(x,t)$ is as follows:

$$\frac{\partial T}{\partial t} = \alpha \frac{\partial^2 T}{\partial x^2} + I_0 e^{-\frac{(x-vt)^2}{r_L^2}}. \tag{21}$$

Due to the non-linearity of the heat source, the above equation can only be solved numerically, as shown in Section 4.4. An analytical solution in the non-closed form of Equation (21) is known, which is as follows [49]:

$$T = T_0 + \frac{q_m}{\pi \rho c_P \sqrt{4\pi\alpha}} \int_0^t \frac{(t-t')}{2\alpha(t-t') + r_L^2} e^{\frac{(x-vt')^2 + y^2}{4\alpha(t-t')^2 + 2r_L^2} - \frac{z^2}{4\alpha(t-t')}} dt'. \tag{22}$$

In this work, however, we use the numerical solution of Equation (21), as described in Section 4.4, as this provides more precise results than Equation (22), since Equation (22) does not consider temperature-dependent material properties, whereas the described numerical simulation does.

4.5.3. Oxidation Kinetics

The diffusion process can be described by Fick’s second law using the following equation:

$$\frac{\partial c}{\partial t} = \frac{\partial}{\partial z} \left(D \frac{\partial c}{\partial z} \right), \tag{23}$$

which establishes a relationship between the temporal concentration gradient $\frac{\partial c}{\partial t}$ and the spatial concentration gradient $\frac{\partial c}{\partial z}$. This also allows the case of transient diffusion processes to be represented. In order to be able to give an analytical solution to Equation (22), a constant diffusion coefficient is assumed, and Fick’s second law is simplified to the following:

$$\frac{\partial c}{\partial t} = D \frac{\partial^2 c}{\partial x^2}. \tag{24}$$

The initial and boundary conditions are defined as follows:

- $c(z, 0) = c_0;$
- $c(0, t) = c_{R0};$
- $\frac{\partial c}{\partial z}(x = L) = 0$ (no flux on the lower side of the substrate thickness).

In order to specify the second boundary condition more precisely, the measured oxygen concentration distribution of the coaxial nozzle from Keller et al. [22] was used. To obtain a function of the boundary oxygen concentration, a regression was carried out which fits the data points with a high degree of agreement ($R^2 = 0.995$). The data points, as well as the fitting function, can be seen in Figure 18.

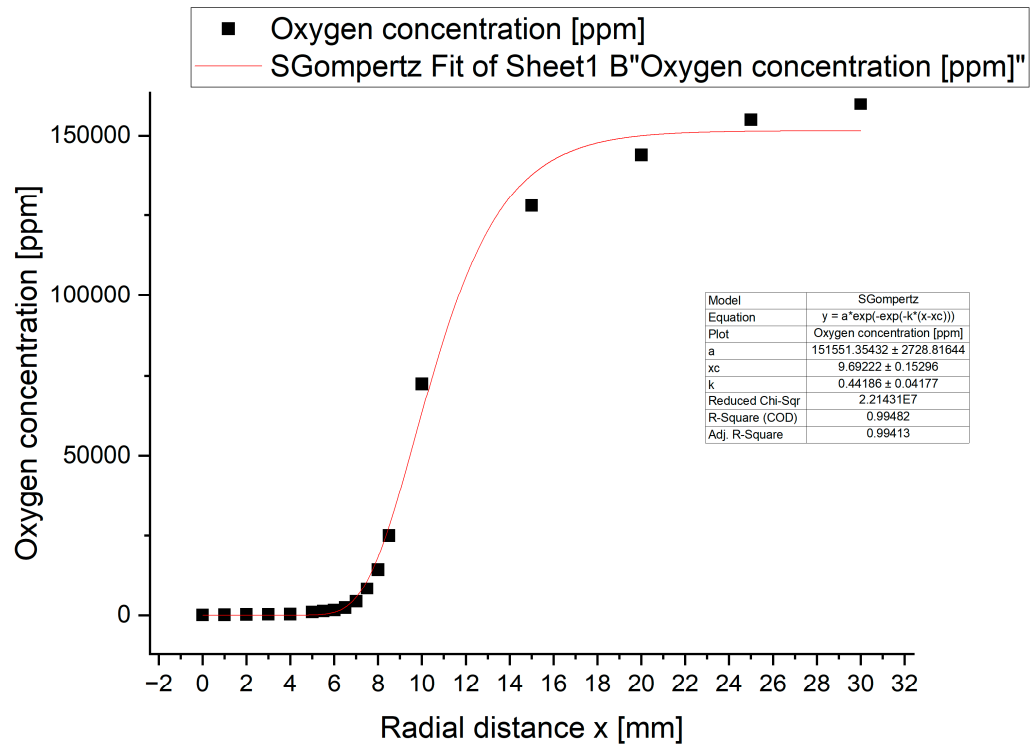


Figure 18. Fitting the boundary oxygen concentration c_{R0} with respect to the radial distance of the nozzle. The nozzle is located at $x = 0$.

As can be seen from Figure 18, the boundary oxygen concentration follows the function shown below:

$$c_{R0}(x) = 151551 \cdot e^{-e^{(-0.442 \cdot (x - 9.69))}} \tag{25}$$

However, this spatial boundary oxygen concentration can be used for DMD processes with a carrier gas to shielding gas volume flow ratio of 4/15. With this specification of the boundary oxygen concentration, a significant distinction is made from the literature [17–21], which allows the titanium samples to oxidize in atmospheric air (e.g., an infinite reservoir of diffusing oxygen). Since the boundary oxygen concentration is non-linear, no closed analytical solution of Equation (24) can be found using the separation of variables approach. A Taylor series expansion, with which the fitting function according to Equation (25) could be approximated linearly, also makes no sense, as the same oxygen concentration would then be obtained for all radial distances x . A different approach is therefore used for modelling the oxidation kinetics. If the oxidation-critical temperature $T_{ox,cr}$ for materials is within the inert gas bell ($x < 5$ mm), oxidation can be neglected as a first approximation. If, on the other hand, the oxidation-critical temperature $T_{ox,cr}$, at which there is no sufficient adhesion of a protective thin oxide layer such as with Ti alloys, is outside the inert gas bell

($x > 5$ mm), the oxygen concentration adsorbed by the metal results from the integral of the nozzle-specific boundary oxygen concentration c_{R0} . This integral is given as follows:

$$\int_0^{x_{T_{ox,cr.}}} c_{R0}(x) dx \quad (26)$$

where $x_{T_{ox,cr.}}$ is the location at which the oxidation-critical temperature is present on the surface of the substrate ($z = 0$). This atmospheric concentration still needs to be converted into a resulting oxygen concentration in the material. This can be undertaken with the help of stoichiometry. The oxygen transfer coefficient Ψ introduced here results from the product of the solution from Equation (25) and the molar mass ratio of the oxygen and the oxygen-absorbing material and is calculated according to the following equation:

$$\Psi = \left[\int_5^{x_{T_{ox,cr.}}} c_{R0}(x) dx \right] \cdot \frac{M_O}{M_{Sub}} \quad (27)$$

where M_O is the molar mass of the oxygen is and M_{Sub} is the molar of the substrate material.

As shown in Section 4.5, the numerical calculation of the temperature field, by solving Equation (21) using the finite element method or the numerical solution of Equation (22) and the subsequent superposition of the spatial oxygen concentration can be used to describe the significant increase in oxidation with the same specific energy input. This way, titanium alloys can be produced with the DMD process that fulfil the oxidation limits and the requirements for the mechanical properties. This means that the oxidation rate can be minimised using the oxidation model presented and can serve as a future guideline for the production of Ti components using DMD. In the future, it is logical to extend the application of the oxidation model and the observed distribution of boundary oxygen concentration to additional materials prone to oxidation, such as aluminium alloys. To achieve this, a heat conduction simulation, akin to the one detailed in this study, would be required, incorporating the specific material parameters (e.g., thermal diffusivity, absorptivity) and identification of the critical temperature for oxidation.

5. Conclusions

The production of Ti6Al4V components using DMD requires suitable process control, not only with regard to the usual process windows considered, which are characterised purely energetically by the supply of a sufficiently high energy input into the substrate, so that a lack of fusion (interlayer porosity) and porosity in the build-up is avoided. This study shows that a holistic approach is required, which, in addition to the exact specification of the temperature field, requires superposition with the spatial oxygen concentration. It is shown that reduced travel speed at the same specific energies increasingly shifts the oxidation-critical area into the region of low oxygen concentration. The present work can be used for the production of components from oxygen affine materials or generally to minimize oxidation during the DMD process. In summary, the following results were achieved in this work:

- The microstructure analysis shows different structures in different areas. This change is due to the different thermal history. The thermally unaffected substrate shows elongated grains, α martensite present in the HAZ and an α -Widmanstätten structure present in columnar β grains. The microstructure shows no dependence on the degree of oxidation.
- Heavily oxidized samples show the highest hardness values, which, however, have insufficient ductility properties.
- Tensile tests show that, by adhering to the oxidation model presented in this work, Ti6Al4V components can be produced using DMD that fulfil the requirements defined in the relevant standards.

- Specific energy is not a sufficient parameter for the production of oxidation affine materials. At the same specific energy, a higher travel speed leads to increasing overheating.
- The varying levels of oxidation can be determined by overlaying the spatial distribution of oxygen concentration at the boundary, with the temperature field calculated numerically using the heat conduction equation. It is important to emphasize that the oxygen concentration profile described by Equation (25) is applicable only under specific conditions: a carrier gas flow rate of 4 L/min and a shielding gas flow rate of 15 L/min. These conditions are critical for establishing an adequate shielding gas environment. From an energetic standpoint, it becomes evident that, for a given specific energy input, reducing the travel speed has a beneficial impact on minimizing oxidation to the lowest extent possible. By meticulously adjusting parameters such as the carrier gas flow rate, shielding gas flow rate, laser power and feed rate, it becomes feasible to mitigate oxidation effectively.

Author Contributions: Conceptualization, D.K. and K.W.; methodology, D.K.; software, D.K.; validation, D.K.; formal analysis, D.K.; investigation, D.K.; resources, K.W.; data curation, D.K. and K.W.; writing—original draft preparation, D.K.; writing—review and editing, K.W.; visualization, D.K.; supervision, K.W.; project administration, D.K. and K.W.; All authors have read and agreed to the published version of the manuscript.

Funding: This research received no external funding.

Data Availability Statement: Dataset available on request from the authors.

Conflicts of Interest: The authors declare no conflict of interest.

References

1. Dilberoglu, U.M.; Gharehpapagh, B.; Yaman, U.; Dolen, M. The Role of Additive Manufacturing in the Era of Industry 4.0. *Procedia Manuf.* **2017**, *11*, 545–554. [\[CrossRef\]](#)
2. Feng, S.C.; Moges, T.; Park, H.; Yakout, M.; Jones, A.T.; Ko, H.; Witherell, P. Functional Requirements of Software Tools for Laser-Based Powder Bed Fusion Additive Manufacturing for Metals. *J. Comput. Inf. Sci. Eng.* **2023**, *23*, 031005. [\[CrossRef\]](#)
3. Dass, A.; Moridi, A. State of the art in directed energy deposition: From additive manufacturing to materials design. *Coatings* **2019**, *9*, 418. [\[CrossRef\]](#)
4. Parimi, L.L.; Ravi, G.A.; Clark, D.; Attallah, M.M. Microstructural and texture development in direct laser fabricated IN718. *Mater. Charact.* **2014**, *89*, 102–111. [\[CrossRef\]](#)
5. Huanes-Alvan, G.E.; Aydogan, B.; Sahasrabudhe, H.; Chakrapani, S.K. Ultrasonic properties of Inconel 718 fabricated via laser-directed energy deposition. *J. Acoust. Soc. Am.* **2020**, *148*, 2648. [\[CrossRef\]](#)
6. Liang, Y.J.; Cheng, X.; Li, J.; Wang, H.M. Microstructural control during laser additive manufacturing of single-crystal nickel-base superalloys: New processing–microstructure maps involving powder feeding. *Mater. Des.* **2017**, *130*, 197–207. [\[CrossRef\]](#)
7. Liu, Y.; Li, A.; Cheng, X.; Zhang, S.Q.; Wang, H.M. Effects of heat treatment on microstructure and tensile properties of laser melting deposited AISI 431 martensitic stainless steel. *Mater. Sci. Eng. A* **2016**, *666*, 27–33. [\[CrossRef\]](#)
8. Dey, I.; Fabbri, M.; Gemmet, S.; Dalae, M.; Wessel, M.; Wegener, K. Manufacturing a prototype with laser direct metal deposition and laser welding made from martensitic steel 1.4313. *Int. J. Adv. Manuf. Technol.* **2023**, *124*, 1993–2009. [\[CrossRef\]](#)
9. Gong, H.; Rafi, K.; Gu, H.; Starr, T.; Stucker, B. Analysis of defect generation in Ti–6Al–4V parts made using powder bed fusion additive manufacturing processes. *Addit. Manuf.* **2014**, *1*, 87–98. [\[CrossRef\]](#)
10. Casadebaigt, A.; Hugues, J.; Monceau, D. High temperature oxidation and embrittlement at 500–600 °C of Ti-6Al-4V alloy fabricated by Laser and Electron Beam Melting. *Corros. Sci.* **2020**, *175*, 108875. [\[CrossRef\]](#)
11. Zwicker, U. *Titan und Titanlegierungen*; Springer: Berlin/Heidelberg, Germany, 2013; Volume 21.
12. Brunette, D.M.; Tengvall, P.; Textor, M.; Thomsen, P. *Titanium in Medicine: Material Science, Surface Science, Engineering, Biological Responses and Medical Applications*; Springer: Berlin, Germany, 2001; p. 232.
13. Ask, M.; Lausmaa, J.; Kasemo, B. Preparation and surface spectroscopic characterization of oxide films on Ti6Al4V. *Appl. Surf. Sci.* **1989**, *35*, 283–301. [\[CrossRef\]](#)
14. Kofstad, P.; Hauffe, K.; Kjollesdal, H.; Siekevitz, P.; Ernster, L.; Diczfalusy, E. Investigation on the oxidation mechanism of titanium. *Acta Chem. Scand.* **1958**, *12*, 239–266. [\[CrossRef\]](#)
15. Latella, B.A.; Gan, B.K.; Li, H. Fracture toughness and adhesion of thermally grown titanium oxide on medical grade pure titanium. *Surf. Coat. Technol.* **2007**, *201*, 6325–6331. [\[CrossRef\]](#)
16. Stringer, J. The oxidation of titanium in oxygen at high temperatures. *Acta Metall.* **1960**, *8*, 758–766. [\[CrossRef\]](#)

17. Gurrappa, I. An oxidation model for predicting the life of titanium alloy components in gas turbine engines. *J. Alloys Compd.* **2005**, *389*, 190–197. [[CrossRef](#)]
18. Wallwork, G.; Smeltzer, W.; Rosa, C. The parabolic oxidation kinetics of alpha-zirconium at 850 °C. *Acta Metall.* **1964**, *12*, 409–415. [[CrossRef](#)]
19. Guleryuz, H.; Cimenoglu, H. Oxidation of Ti–6Al–4V alloy. *J. Alloys Compd.* **2009**, *472*, 241–246. [[CrossRef](#)]
20. Yu, C.; Zhu, S.; Wei, D.; Wang, F. Oxidation and H₂O/NaCl-induced corrosion behavior of sputtered Ni–Si coatings on Ti6Al4V at 600–650 °C. *Surf. Coat. Technol.* **2007**, *201*, 7530–7537. [[CrossRef](#)]
21. Coddet, C.; Craze, A.M.; Beranger, G. Measurements of the adhesion of thermal oxide films: Application to the oxidation of titanium. *J. Mater. Sci.* **1987**, *22*, 2969–2974. [[CrossRef](#)]
22. Keller, D.; Monney, A.; Schudeleit, T.; Wegener, K. Spatial Oxygen Distribution of the Direct Metal Deposition Process for Different Powder Nozzles. *Appl. Sci.* **2023**, *13*, 9470. [[CrossRef](#)]
23. Keller, D.; Monney, A.; Wirth, F.; Wegener, K. Oxygen Uptake of Ti6Al4V during Direct Metal Deposition Process. *Metals* **2024**, *14*, 119. [[CrossRef](#)]
24. *DIN EN ISO 6507-1: 2018-07*; Metallische Werkstoffe—Härteprüfung nach Vickers—Teil_1: Prüfverfahren (ISO_6507-1: 2018). Deutsches Institut für Normung: Berlin, Germany, 2018.
25. Beerli, T.; Roth, C.C.; Mohr, D. Semi-automatic miniature specimen testing method to characterize the plasticity and fracture properties of metals. *Acta Mater.* **2024**, *263*, 119539. [[CrossRef](#)]
26. Soffel, F.; Lin, Y.; Keller, D.; Egorov, S.; Wegener, K. Laser Remelting Process Simulation and Optimization for Additive Manufacturing of Nickel-Based Super Alloys. *Materials* **2021**, *15*, 177. [[CrossRef](#)] [[PubMed](#)]
27. Wirth, F.; Wegener, K. A physical modeling and predictive simulation of the laser cladding process. *Addit. Manuf.* **2018**, *22*, 307–319. [[CrossRef](#)]
28. Boivineau, M.; Cagran, C.; Doytier, D.; Eyraud, V.; Nadal, M.-H.; Wilthan, B.; Pottlacher, G. Thermophysical properties of solid and liquid Ti-6Al-4V (TA6V) alloy. *Int. J. Thermophys.* **2006**, *27*, 507–529. [[CrossRef](#)]
29. Mills, K.C. *Recommended Values of Thermophysical Properties for Selected Commercial Alloys*; Woodhead Publishing: Thorston, UK, 2002.
30. Katinas, C.; Liu, S.; Shin, Y.C. Self-sufficient modeling of single track deposition of Ti–6Al–4V with the prediction of capture efficiency. *J. Manuf. Sci. Eng.* **2019**, *141*, 011001. [[CrossRef](#)]
31. Yang, J.; Sun, S.; Brandt, M.; Yan, W. Experimental investigation and 3D finite element prediction of the heat affected zone during laser assisted machining of Ti6Al4V alloy. *J. Mater. Process. Technol.* **2010**, *210*, 2215–2222. [[CrossRef](#)]
32. Lu, X.; Lin, X.; Chiumenti, M.; Cervera, M.; Hu, Y.; Ji, X.; Ma, L.; Yang, H.; Huang, W. Residual stress and distortion of rectangular and S-shaped Ti-6Al-4V parts by Directed Energy Deposition: Modelling and experimental calibration. *Addit. Manuf.* **2019**, *26*, 166–179. [[CrossRef](#)]
33. Westerberg, K.W.; Merier, T.C.; McClelland, M.A.; Braun, D.G.; Berzins, L.V.; Anklam, T.M.; Storer, J. Analysis of the e-Beam Evaporation of Titanium and Ti-6Al-4V Lawrence Livermore National Lab. (LLNL): Livermore, CA, USA, 1998.
34. Nair, A.M.; Muvvala, G.; Sarkar, S.; Nath, A.K. Real-time detection of cooling rate using pyrometers in tandem in laser material processing and directed energy deposition. *Mater. Lett.* **2020**, *277*, 128330. [[CrossRef](#)]
35. Fan, D.; Chen, L.Q.; Chen, S.P. Effect of grain boundary width on grain growth in a diffuse-interface field model. *Mater. Sci. Eng. A* **1997**, *238*, 78–84. [[CrossRef](#)]
36. Bambach, M.; Sizova, I.; Sydow, B.; Hemes, S.; Meiners, F. Hybrid manufacturing of components from Ti-6Al-4V by metal forming and wire-arc additive manufacturing. *J. Mater. Process. Technol.* **2020**, *282*, 116689. [[CrossRef](#)]
37. Hass, G. Preparation, structure, and applications of thin films of silicon monoxide and titanium dioxide. *J. Am. Ceram. Soc.* **1950**, *33*, 353–360. [[CrossRef](#)]
38. Kubaschewski, O.; Hopkins, B.E. *Oxidation of Metals and Alloys*; London Butterworths: Oxford, UK, 1962; pp. 286, 287, 425, 433.
39. Andreeva, V.V. Behavior and nature of thin oxide films on some metals in gaseous media and in electrolyte solutions. *Corrosion* **1964**, *20*, 35t–46t. [[CrossRef](#)]
40. Mindel, M.J.; Pollack, S.R. The room temperature oxidation of titanium thin films. *Acta Met.* **1969**, *17*, 1441–1448. [[CrossRef](#)]
41. Hickman, J.W.; Gulbransen, E.A. Oxide films formed on titanium, zirconium, and their alloys with nickel, copper, and cobalt. *Anal. Chem.* **1948**, *20*, 158–165. [[CrossRef](#)]
42. Jenkins, A. The oxidation of titanium at high temperatures in an atmosphere of pure oxygen. *J. Inst. Met.* **1953**, *82*, 213–221.
43. Hurlen, T.; Wilhelmsen, W. Passive behaviour of titanium. *Electrochim. Acta* **1986**, *31*, 1139–1146. [[CrossRef](#)]
44. Davies, M.H.; Birchenall, C.E. Oxidation of titanium. *JOM* **1951**, *3*, 877–880. [[CrossRef](#)]
45. Richardson, L.S.; Grant, N.J. Reaction of oxygen and nitrogen with titanium from 700 °C to 1050 °C. *JOM* **1954**, *6*, 69–70. [[CrossRef](#)]
46. Kofstad, P.; Haufler, K. Oxydation von titan. *Mater. Corros.* **1956**, *7*, 642–649. [[CrossRef](#)]
47. Grant, F.A. Properties of rutile (*Titanium dioxide*). *Rev. Mod. Phys.* **1959**, *31*, 646–674. [[CrossRef](#)]

-
48. Mortimer, C.E.; Müller, U. *Chemie: Das Basiswissen der Chemie*; 126 Tabellen; Georg Thieme Verlag: Stuttgart, Germany, 2007.
 49. Eagar, T.W.; Tsai, N.S. Temperature fields produced by traveling distributed heat sources. *Weld. J.* **1983**, *62*, 346–355.

Disclaimer/Publisher's Note: The statements, opinions and data contained in all publications are solely those of the individual author(s) and contributor(s) and not of MDPI and/or the editor(s). MDPI and/or the editor(s) disclaim responsibility for any injury to people or property resulting from any ideas, methods, instructions or products referred to in the content.